# Evolution of the Structure and Thermodynamic Stability of the $BaTiO_3(001)$ Surface

Alexie M. Kolpak,[1] Dongbo Li,[2] Rui Shao,[2] Andrew M. Rappe,[1] and Dawn A. Bonnell[2]
[1]*The Makineni Theoretical Laboratories, Department of Chemistry, University of Pennsylvania, Philadelphia, Pennsylvania 19104-6323, USA*
[2]*Department of Materials Science and Engineering, University of Pennsylvania, Philadelphia, Pennsylvania 19104, USA*

(Received 28 January 2008; published 16 July 2008)

We report a series of new surface reconstructions on $BaTiO_3(001)$ as a function of environmental conditions, determined via scanning tunneling microscopy and low energy electron diffraction. Using density functional theory calculations and thermodynamic modeling, we construct a surface phase diagram and determine the atomic structures of the thermodynamically stable phases. Excellent agreement is found between the predicted phase diagram and experiment. The results enable prediction of surface structures and properties under the entire range of accessible environmental conditions.

DOI: 10.1103/PhysRevLett.101.036102 PACS numbers: 68.35.Md, 68.37.Ps, 68.47.Gh

Oxides play a vital role in numerous applications, including electronic ceramics, semiconductor technology, and catalysis. Knowledge of the atomic structure and properties of oxide surfaces is essential in understanding and predicting the behavior of such systems, particularly as novel integrated nanodevices are developed. Surfaces are highly sensitive to environmental conditions, resulting in a large number of atomic structures (reconstructions). Such reconstructions are often produced by thermochemical conditions that are not entirely controlled; consequently, it is not easy to distinguish between stable and metastable structures.

Much research has focused on the $SrTiO_3(001)$ surface [1–11], which has been shown to adopt reconstructions with $(1 \times 1)$, $(2 \times 1)$, $c(4 \times 2)$, $c(4 \times 4)$, $c(6 \times 2)$, $(\sqrt{5} \times \sqrt{5})R26.6^\circ$, and $(2 \times 2)$ symmetries. Larger superstructures have also been observed [11–14]. Even for this well-studied surface, variation in experimental conditions has resulted in conflicting observations, and only a limited number of structures, primarily $(1 \times 1)$ and $(2 \times 1)$ surfaces, have been treated theoretically [15–18]. Evidence suggests that $BaTiO_3$ surfaces will also adopt complex surface reconstructions: both $(2 \times 1)$ [19] and $(\sqrt{5} \times \sqrt{5})R26.6^\circ$ reconstructions have been observed on the (001) surface [20,21], and various superstructures were found on the (111) surface [22]. Theoretical studies of the $BaTiO_3(001)$ surfaces have focused on stoichiometric $(1 \times 1)$ BaO- and $TiO_2$-terminated surfaces [23,24] and a few O-vacancy reconstructions [25].

Here, we experimentally and theoretically determine the surface structure of $BaTiO_3(001)$ over a wide range of environmental conditions, quantifying stability limits of each reconstruction. Using scanning tunneling microscopy (STM) and low energy electron diffraction (LEED), a series of surface reconstructions including $(1 \times 1)$, $(2 \times 1)$, $c(2 \times 2)$, $(2 \times 2)$, $(\sqrt{5} \times \sqrt{5})R26.6^\circ$, $(3 \times 1)$, $(3 \times 2)$, and $(6 \times 1)$ surfaces, are observed here, most for the first time. Using density functional theory (DFT) and *ab initio* thermodynamics, we compute the atomic structures and free energies of >70 possible $BaTiO_3(001)$ reconstructions, and predict the phase diagram of the $BaTiO_3(001)$ surface. Excellent agreement between theory and experiment provides a coherent explanation for surface evolution.

Single crystal $BaTiO_3(001)$ substrates were preannealed in a tube furnace at 1223–1273 K in high purity oxygen, and then in reducing $H_2$ or ultrahigh vacuum (UHV) environment; the latter step creates bulk oxygen vacancies, giving rise to electrical conductivity enabling STM, LEED and AES. Samples were introduced into the UHV chamber (Omicron, VT-AFM), where they were annealed at temperatures ranging from 973 K to 1573 K. Sample heating was conducted by passing a current through the substrate, and surface temperatures were measured with an optical pyrometer. The STM measurements were performed with etched tungsten tips in constant current mode with biases $\approx$1–2 V and currents of 0.1–0.2 nA. The base pressure of the system was $10^{-8}$–$10^{-9}$ Torr during sample heating and $\approx 10^{-10}$ Torr during imaging. Images were obtained at room temperature.

DFT calculations were performed with ultrasoft pseudopotentials [26] and the generalized gradient approximation as implemented in the *ab initio* code DACAPO [27], with a 30 Ry plane wave cutoff and a $4 \times 4 \times 1$ Monkhorst-Pack $k$-point mesh. To simulate the surface of a thick film, the systems were composed of 5–6 layers of bulk paraelectric $BaTiO_3$ (for BaO and $TiO_2$ surface terminations, respectively), capped on one end by three layers of Pt metal [28]. The capping Pt layers and the bottom 3–4 atomic layers of $BaTiO_3$ were held fixed in the bulk paraelectric structure. The top $BaTiO_3$ stoichiometric unit, plus any adsorbed species were relaxed completely until forces were <1 meV/nm. A dipole correction was included in the 1.2 nm vacuum separating the film from its periodic image. The in-plane lattice constant was fixed to the theoretical bulk $BaTiO_3$ value ($a = 0.399$ nm). $(1 \times 1)$, $(2 \times 1)$, $c(2 \times 2)$, $(2 \times 2)$, and $(3 \times 1)$ surface supercells were considered, with various coverages and patterns composed of O vacancies, Ba, Ti, or O ad-atoms, or additional $Ti_xO_y$ or $Ba_xO_y$ layers.

A diagram of the annealing temperatures and observed reconstructions is shown in Fig. 2(a). All surfaces exhibit atomically flat terraces, with unit-cell (0.4 nm) step heights, indicating the presence of a single surface termination. The $(1 \times 1)$, $(2 \times 1)$, $c(2 \times 2)$, $(2 \times 2)$, $(\sqrt{5} \times \sqrt{5})R26.6^\circ$, $(3 \times 1)$, $(3 \times 2)$, and $(6 \times 1)$ reconstructions were characterized by LEED and several were imaged by STM. Except for the $(2 \times 1)$ and $(\sqrt{5} \times \sqrt{5})R26.6^\circ$ reconstructions, these reconstructions, and more importantly, the relationships between them, are reported here for the first time.

Preannealed crystals exhibit faint $(1 \times 1)$ LEED patterns, with no contaminants detectable by Auger electron spectroscopy (AES). Heating between 873–973 K for 30 min in UHV results in $(2 \times 1)$ or $c(2 \times 2)$ reconstructions. Higher $T$ annealing at 973–1073 K for 30 min leads to weak $(\frac{1}{4}, \frac{1}{4})$ spots in the LEED pattern, indicative of a $c(4 \times 4)$ reconstruction. For initial UHV annealing temperatures of 1273 K, $(2 \times 2)$, $(\sqrt{5} \times \sqrt{5})R26.6^\circ$, and $(3 \times 1)$ superstructures develop as $T$ is increased to 1473 K. Interestingly, the $(\sqrt{5} \times \sqrt{5})R26.6^\circ$ and $(3 \times 1)$ reconstructions coexist for short times at 1323–1373 K. Figure 1 illustrates the structural characterization of the $(\sqrt{5} \times \sqrt{5})R26.6^\circ$ and $(3 \times 1)$ reconstructions. The dimensions of the unit cells determined by LEED and STM agree. The STM image of the $(\sqrt{5} \times \sqrt{5})R26.6^\circ$ reconstruction in Fig. 1(a) consists of two domains rotated by 36.5° with respect to each other. Multiple domain orientations are also identified in the LEED pattern. Figure 1(b) shows the STM image of the $(3 \times 1)$ surface, exhibiting bright rows believed to be adatoms along the [100] direction. The average spacing between adjacent rows is 1.2 nm, in agreement with the $(3 \times 1)$ unit-cell dimension.

Aggressive annealing above 1373–1473 K results in continuously evolving surface morphologies on microscopic as well as nanoscopic length scales. The changing nature of the surface indicates that some of the structures are not thermodynamically stable. Below 1273 K, where the reconstructions appear to be thermodynamically stable, the surface is atomically flat with single-unit-cell high steps running along the [100] directions. Based on findings for $SrTiO_3$ surfaces, this [100] step alignment is suggestive of the dominance of $TiO_2$ surface planes; our DFT calculations also find that $TiO_2$ surfaces are more favorable than BaO surfaces under most conditions. With annealing above 1373 K, a stripe phase oriented along the [100] direction develops subsequent to the $(3 \times 1)$ reconstruction, increasing in coverage with time and temperature [Fig. 1(e)]. Continued annealing at 1473 K results in the development of a $(1 \times 1)$ surface. At some locations macroscopic precipitates occur, as can be seen in Fig. 1(f).

DFT was used to model more than 70 possible BaO- and $TiO_2$-terminated surface structures, the details of which are reported elsewhere. The Gibbs free energy of each structure, $\gamma(T, p) = G_{\mathrm{surf}} - n_{\mathrm{Ba}}\mu_{\mathrm{Ba}} - n_{\mathrm{Ti}}\mu_{\mathrm{Ti}} - n_{\mathrm{O}}\mu_{\mathrm{O}}$, was computed, where $G_{\mathrm{surf}}$ is the free energy of the slab, $\mu_{\mathrm{Ba}}$, $\mu_{\mathrm{Ti}}$, and $\mu_{\mathrm{O}}$ are the chemical potentials of Ba, Ti, and O, respectively, and $n_{\mathrm{Ba}}$, $n_{\mathrm{Ti}}$, and $n_{\mathrm{O}}$ are the number of Ba, Ti, and O atoms in the surface [29]. $G_{\mathrm{surf}}$ is well approximated from DFT total energies [30], assuming the entropy change of the slab is approximately the same as that of its components in bulk form: $G_{\mathrm{surf}} = E_{\mathrm{surf}} - n_{\mathrm{Ba}}E_{\mathrm{Ba}}^{\mathrm{bulk}} - n_{\mathrm{Ti}}E_{\mathrm{Ti}}^{\mathrm{bulk}} - n_{\mathrm{O}}\frac{1}{2}E_{\mathrm{O}_2}^{\mathrm{iso}}$, where $E_{\mathrm{surf}} = E_{\mathrm{slab}}^{\mathrm{tot}} - E_{\mathrm{base}} - n_{\mathrm{bulk}}$, $E_{\mathrm{slab}}^{\mathrm{tot}}$ and $E_{\mathrm{base}}$ are the total energies of the slab and the fixed base, $E_{\mathrm{BaTiO}_3}^{\mathrm{bulk}}$, $E_{\mathrm{Ba}}^{\mathrm{bulk}}$ and $E_{\mathrm{Ti}}^{\mathrm{bulk}}$ are the total energies per unit cell of bulk $BaTiO_3$, Ba, and Ti, respectively, and $E_{\mathrm{O}_2}^{\mathrm{iso}}$ is the total energy of an isolated $O_2$ molecule [31].

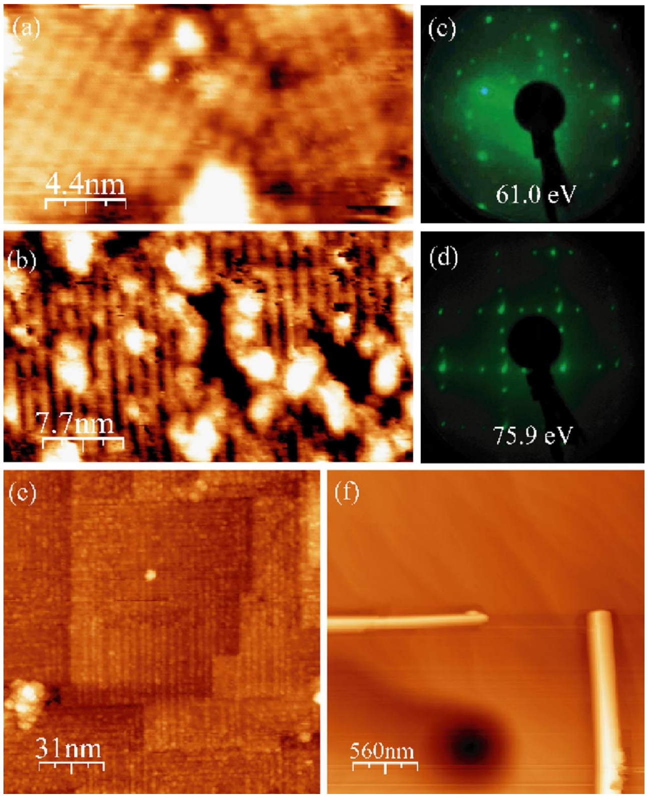

FIG. 1 (color online). STM images of (a) $(\sqrt{5} \times \sqrt{5})R26.6^\circ$ and (b) $(3 \times 1)$ reconstructions. LEED patterns of the (c) $(\sqrt{5} \times \sqrt{5})R26.6^\circ$ and (d) $(3 \times 1)$ $BaTiO_3(001)$ surfaces. (e) STM image of nanometer wide stripes on the flat terraces upon annealing above 1373 K. (f) Precipitation on nano-stripe-ordered surface after aggressive annealing for a prolonged time.

The effect of $\mu_{\mathrm{O}}$ and $\mu_{\mathrm{Ba}}$ on structural stability is illustrated in the theoretical surface phase diagram in Fig. 2. The diagram defines stabilities for the lowest energy surface structures; superimposed are the stability limits of bulk $BaTiO_3$ at relevant $T$. The figure shows seven thermodynamically stable surface structures in five different symmetries in the region of $BaTiO_3$ stability. The boundaries of this region are defined by the equilibria of bulk $BaTiO_3$ with $Ba_xO_y$ and $Ti_xO_y$ and the following constraints: (i) Bulk $BaTiO_3$ is in equilibrium with the surface, so the Gibbs free energy of bulk $BaTiO_3$ is always $g^{\mathrm{bulk}}_{\mathrm{BaTiO_3}}(T, p) = \mu_{\mathrm{Ba}}(T, p) + \mu_{\mathrm{Ti}}(T, p) + 3\mu_{\mathrm{O}}(T, p)$; (ii) a small amount of water is always present (as is the case in UHV), so $\mu_{\mathrm{O}}(T, p) + 2\mu_{\mathrm{H}}(T, p) \geq g_{\mathrm{H_2O}}(T, p)$; and (iii) as a result of preannealing in $H_2$, $\mu_{\mathrm{H}} = 0.0$, giving the lower bound of the oxygen chemical potential as $\mu^{\mathrm{min}}_{\mathrm{O}} = g^{0}_{\mathrm{H_2O}}(T)$.

The temperature dependence of the Gibbs free energies is explicitly included via experimentally tabulated values. Previous studies have neglected this $T$ dependence [16,17]. However, as Fig. 2 indicates, including the $T$-dependence significantly extends the region of $BaTiO_3$ stability, and is crucial to understanding the evolution of the surface.

Knowledge of the oxygen partial pressure defines the value of $\mu_{\mathrm{O}}$ at every $T$. The equilibrium partial pressures of Ba and Ti with their respective binary oxides, along with the time scale of the experiments, suggest that in the experimental temperature range the system will reside at the boundary between BaO and $BaTiO_3$ stability. Consequently, $\mu_{\mathrm{Ba}}$ is also defined, providing sufficient information to determine the trajectory of the system through phase space and to relate each experimental observation to a point in the surface phase diagram. The yellow arrow in Fig. 2 shows the computed trajectory for $p_{\mathrm{O_2}} = 10^{-10}$ torr (the upper limit of the oxygen partial pressure in the UHV chamber), while the black arrow gives the trajectory at $p_{\mathrm{O_2}} = 10^{-27}$ torr (the lower limit of the oxygen partial pressure, corresponding $\mu^{\mathrm{min}}_{\mathrm{O}}(T, p)$. The actual pathway is expected to be somewhere in between the two limits, in good agreement with the experimental observations.

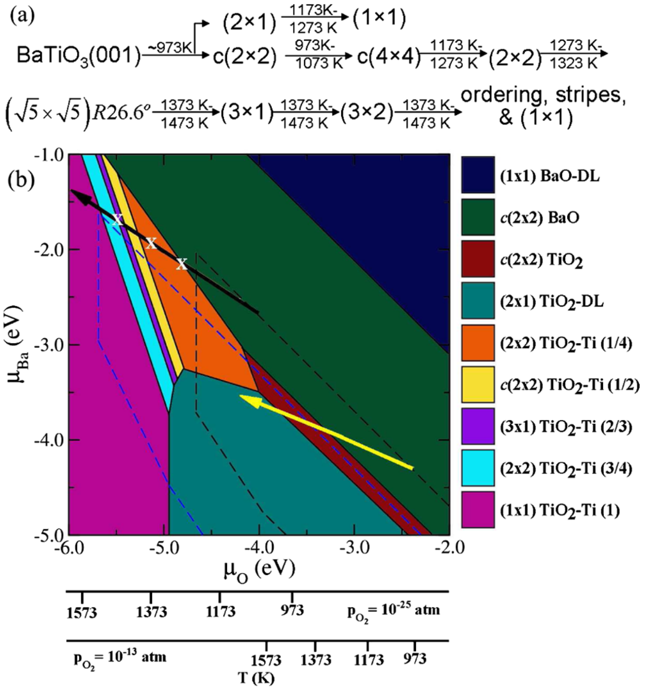

FIG. 2 (color online). (a) Schematic of annealing sequence and observed phases. (b) Computed surface phase diagram of $BaTiO_3$. The black and blue dashed lines show the boundaries of $BaTiO_3$ bulk stability $T = 1000$ K and $T = 1400$ K, respectively. The black and yellow arrows show the computed trajectories through phase space for the lower and upper limits of $p_{\mathrm{O_2}}$, respectively, (see text). The white X's correspond to experimental observations along the low $p_{\mathrm{O_2}}$ trajectory.

The phase diagram can be used to explain the relationships between various equilibrium phases and nonequilibrium morphologies. Following the black arrow in Fig. 2, $\mu_{\mathrm{O}}$ decreases and the surface goes through a series of reconstructions with increasing Ti coverage, $\theta$, as the temperature is increased: $(2 \times 2) \rightarrow c(2 \times 2) \rightarrow (3 \times 1) \rightarrow (2 \times 2) \rightarrow (1 \times 1)$ $(\theta = \frac{1}{4}, \frac{1}{2}, \frac{2}{3}, \frac{3}{4}, 1)$. On the other hand, at lower $\mu_{\mathrm{Ba}}$ the surface reconstructs directly from the $(2 \times 1)$ to the $(1 \times 1)$ phase under the same range of $\mu_{\mathrm{O}}$. The low temperature $c(2 \times 2)$ and $(2 \times 1)$ and the high temperature $(2 \times 2)$ and $(3 \times 1)$ phases occur within the $BaTiO_3$ stability region as predicted. Two other phases, $c(4 \times 4)$ and $(\sqrt{5} \times \sqrt{5})R26.6°$, are observed experimentally but have not been calculated due to computational time constraints. Following the stability trends, the theoretical phase fields of these structures would be located in the region between $c(2 \times 2)$ and $(3 \times 1)$, exactly the region indicated by experiment.

Under high temperature conditions in which $BaTiO_3$ is not stable, i.e., outside of the dashed lines in Fig. 2, the surface undergoes a decomposition reaction: Evaporation of BaO drives the rearrangement of Ti and O atoms on the surface to form some energetically stable $Ti_xO_y$-rich surface phase. The ordered nanostripes occurring at the highly annealed surfaces shown in Fig. 1(e) are attributed to this mechanism. Returning from such an excursion (lowering $T$) results in BaO precipitation. These precipitates cannot find the $BaTiO_3$ structure without considerable annealing and therefore aggregate in micrometer-sized BaO clusters, Fig. 1(f).

The phase relations in Fig. 2 explain the order of experimentally observed reconstructions and the surface phase composition, but STM images alone cannot determine the atomic structure of the surfaces. To relate the image contrast to atom positions we computed the local density of states (LDOS) with energy between the Fermi level and 2 eV above the conduction band edge, summing over all $z$ to obtain an image of the $xy$ plane [32]. The atomic structure of the only thermodynamically stable $(3 \times 1)$ phase determined from a wide array of computed $(3 \times 1)$ surfaces is shown in Fig. 3(c). The reconstruction consists of Ti atoms at 2/3 of the empty hollow sites in the oxygen lattice (i.e., above the Ba atoms in the subsurface layer) and the upward shift of 1/2 of the surface oxygen atoms (see supplementary material [33]). Because of the Ti $d$ character of the conduction band edge, the Ti adatoms, which are ≈1 Å higher than the Ti atoms in the stoichiometric $TiO_2$ plane, are responsible for the bright spots in the STM image [Fig. 3(b)]. At lower resolution [Fig. 3(a)], these spots appear as stripes twice the width of the dark

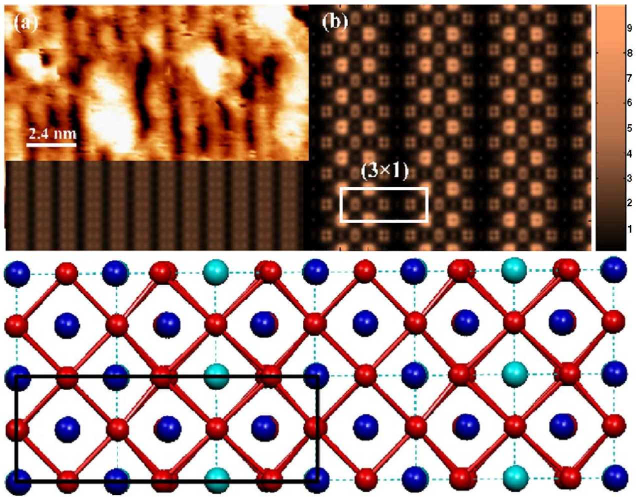

FIG. 3 (color online). (a) Comparison of STM and the computed LDOS of the predicted $(3 \times 1)$ phase. (b) Atomic scale detail of the computed LDOS and (c) surface atomic structure for the same phase. Ba: cyan, Ti: blue, O: red. The color bar in (b) gives the intensity in arbitrary units.

stripes, as observed in the experimental images. The agreement provides strong evidence that the 2/3 coverage Ti structure is responsible for the observed $(3 \times 1)$ reconstruction.

We have reported a family of related $BaTiO_3(001)$ surfaces. *Ab initio* thermodynamic calculations predict the surface phase diagram, which is confirmed by experiment. A comparison of STM image contrast with local density of states variations calculated for the proposed atomic structures are in good agreement, further confirming the phase diagram. These results represent the first comprehensive analysis of a family of oxide reconstructions that includes atomic structure as well as thermodynamic stability, enabling prediction of equilibrium structures and understanding of nonequilibrium morphologies.

The authors acknowledge support from the U. S. National Science Foundation MRSEC No. DMR 05-20020. D. B. L., R. S., and D. A. B. also acknowledge the facilities support from the Nano/Bio Interface Center No. DMR00-80863 and DMR04-25780. A. M. K. and A. M. R. also acknowledge support from the Department of Energy Office of Basic Energy Sciences, under Grant No. DE-FG02-07ER15920 and the Air Force Office of Scientific Research, Air Force Materiel Command, USAF, under Grant No. FA9550-07-1-0397, as well as computational support from the High-Performance Computing Modernization Office of the U. S. Department of Defense.

---

[1] M. R. Castell, Surf. Sci. **505**, 1 (2002).
[2] N. Erdman and L. D. Marks, Surf. Sci. **526**, 107 (2003).
[3] N. Erdman, K. R. Poeppelmeier, M. Asta, O. Warschkow, D. E. Ellis, and L. D. Marks, Nature (London) **419**, 55 (2002).
[4] R. Herger, P. R. Willmot, O. Bunk, C. M. Schlepütz, B. D. Patterson, and B. Delley, Phys. Rev. Lett. **98**, 076102 (2007).
[5] Q. D. Jiang and J. Zegenhagen, Surf. Sci. **425**, 343 (1999).
[6] T. Kubo and H. Nozoye, Phys. Rev. Lett. **86**, 1801 (2001).
[7] T. Kubo and H. Nozoye, Surf. Sci. **542**, 177 (2003).
[8] D. T. Newell, A. F. Harrison, F. Silly, and M. R. Castell, Phys. Rev. B **75**, 205429 (2007).
[9] F. Silly, D. T. Newell, and M. R. Castell, Surf. Sci. Lett. **600**, 219 (2006).
[10] K. Szot and W. Speier, Phys. Rev. B **60**, 5909 (1999).
[11] V. Vonk, S. Konings, G. J. van Hummel, S. Harkema, and H. Graafsma, Surf. Sci. **595**, 183 (2005).
[12] M. R. Castell, Surf. Sci. **516**, 33 (2002).
[13] F. Silly and M. R. Castell, Appl. Phys. Lett. **85**, 3223 (2004).
[14] D. S. Deak, F. Silly, D. T. Newell, and M. R. Castell, J. Phys. Chem. B **110**, 9246 (2006).
[15] O. Warschkow, M. Asta, N. Erdman, K. R. Poeppelmeier, D. E. Ellis, and L. D. Marks, Surf. Sci. **573**, 446 (2004).
[16] K. Johnston, M. R. Castell, A. T. Paxton, and M. W. Finnis, Phys. Rev. B **70**, 085415 (2004).
[17] E. Heifets, S. Piskunov, E. A. Kotomin, Y. F. Zhukovskii, and D. E. Ellis, Phys. Rev. B **75**, 115417 (2007).
[18] L. M. Liborio, C. G. Sanchez, A. T. Paxton, and M. W. Finnis, J. Phys. Condens. Matter **17**, L223 (2005).
[19] R. Courths, Phys. Status Solidi B **100**, 135 (1980).
[20] H. Bando, T. Shimitzu, Y. Aiural, Y. Haruyama, K. Oka, and Y. Nishihara, J. Vac. Sci. Technol. B **14**, 1060 (1996).
[21] T. Shimizu, H. Bando, Y. Aiural, Y. Haruyama, K. Oka, and Y. Nishihara, Jpn. J. Appl. Phys., Part 2 **34**, L1305 (1995).
[22] C. Hagendorf, K. M. Schindler, T. Doege, and H. Neddermeyer, Surf. Sci. **436**, 121 (1999).
[23] R. I. Eglitis, G. Borstel, E. Heifets, S. Piskunov, and E. Kotomin, J. Electroceram. **16**, 289 (2006).
[24] S. Piskunov, and E. A. Kotomin, and E. Heifets, Microelectron. Eng. **81**, 472 (2005).
[25] M. Q. Cai, Y. J. Zhang, G. W. Yang, Z. Yin, M.-S. Zhang, W.-Y. Hu, and Y.-G. Wang, J. Chem. Phys. **124** 174701 (2006).
[26] D. Vanderbilt, Phys. Rev. B **41**, 7892(R) (1990).
[27] http://dcwww.camp.dtu.dk/campos/Dacapo/.
[28] The convergence of the surface energy, atomic structure, and DOS was confirmed by comparison to symmetric converged thick $BaTiO_3$ slabs.
[29] The chemical potentials are defined with respect to the total energy of the most stable phase of the element at $T = 0$ K and $p = 1$ atm, i.e., Ba and Ti metals and $O_2$ gas.
[30] K. Reuter and M. Scheffler, Phys. Rev. B **65**, 035406 (2001).
[31] $E_{O_2}^{\mathrm{iso}}$ is corrected for the known DFT error in the bond energy, such that $E_{O_2}^{\mathrm{iso}} = 2E_O + E_{\mathrm{bond}}^{\mathrm{expt}}$.
[32] Decay of the STM signal was modeled by multiplying the LDOS by $e^{(z_{\mathrm{tip}}-z)}$, where $z_{\mathrm{tip}}$, the distance between the tip and the sample surface, was 2 Å above the topmost surface atom.
[33] See EPAPS Document No. E-PRLTAO-101-022829 for further structural details and side views of the proposed $(3 \times 1)$ phase. For more information on EPAPS, see http://www.aip.org/pubservs/epaps.html.